



# A new purification method for carbon nanotubes and associated atomic force microscope force–distance curve analysis

Chuan He<sup>a,\*</sup>, Yuzhi Hao<sup>a</sup>, Hongbo Zeng<sup>c</sup>, Tian Tang<sup>d</sup>, James Xing<sup>f</sup>, Jie Chen<sup>a,b,e</sup>

<sup>a</sup> Department of Electrical and Computer Engineering, University of Alberta, Edmonton, Alberta, Canada

<sup>b</sup> Department of Biomedical Engineering, University of Alberta, Edmonton, Alberta, Canada

<sup>c</sup> Department of Chemical and Materials Engineering, University of Alberta, Edmonton, Alberta, Canada

<sup>d</sup> Department of Mechanical Engineering, University of Alberta, Edmonton, Alberta, Canada

<sup>e</sup> National Institute for Nanotechnology, Edmonton, Alberta, Canada

<sup>f</sup> Department of Laboratory Medicine & Pathology, University of Alberta, Edmonton, Alberta, Canada

## ARTICLE INFO

### Article history:

Received 7 April 2011

Received in revised form 15 July 2011

Accepted 18 July 2011

Available online 23 July 2011

### Keywords:

Magnetic SWNTs

AFM force curve

JKR model

Purification

## ABSTRACT

The discovery of carbon nanotubes has opened numerous cutting-edge nanoscale research fields, such as microelectronic devices and biomedical applications. Although pure nanotubes suffice for most purposes, highly purified magnetic carbon nanotubes are more suitable for specialized applications such as gene delivery. The conventional methods of purification are too harsh for nanotubes to retain their magnetic properties, hence it requires loading of magnetic nanoparticles inside individual tubes. In this paper, we propose an innovative purification method to directly extract magnetic carbon nanotubes from arc-discharged single-walled carbon nanotubes. The procedure is easy, and atomic force microscope (AFM) force–distance curve analysis combined with transmission electron microscopy (TEM) images are used to monitor the purification process. The AFM force–distance curves present the forces between the AFM tip and different sample surfaces. By comparing the peak values on a series of curves associated with different sample points, we can directly differentiate the carbon nanotubes retaining magnetic characteristics from other nanotubes after the purification process.

© 2011 Elsevier B.V. All rights reserved.

## 1. Introduction

Since Iijima discovered carbon nanotubes (CNTs) in 1991 [1], interest in utilizing CNTs has exponentially increased. Current research on CNTs can be found in a wide range of areas, such as microelectronics [2], renewable energy [3], and biomedicine [4]. In most cases, purified CNTs are required. Pantarotto reported increased gene delivery efficiency by applying CNT as a proper transporter [4], while Chen has shown that magnetic single-walled carbon nanotubes (SWNTs) enhance guided penetration into hard-to-deliver cell lines, such as stem cells [5]. To modify CNTs with magnetic materials, there are two methods. The first method is to load magnetic nanoparticles inside CNTs, but this requires the diameter of the CNT to be around 300 nm which is too large for application in *in vitro* study [6]. The other way is to purify CNTs manufactured by chemical vapour deposition (CVD) method. According to Cai's work, CVD produced CNTs usually have embedded magnetic nanoparticles inside the CNTs. The diameter of these CNTs is much smaller, around 100 nm [7].

\* Corresponding author.

E-mail address: [chuan.he@ualberta.ca](mailto:chuan.he@ualberta.ca) (C. He).

In this work, we describe an innovative purification method to obtain magnetic carbon nanotubes (M-CNTs) from arc-discharged SWNTs. The arc discharge technology requires two electrodes placed in a gaseous atmosphere where a direct current (DC) passes through. The production of SWNTs usually requires the insertion of a mixture of metallic catalysts into the anode [1]. As a result, metallic catalyst nanoparticles such as nickel always remain in produced SWNTs as impurities; some of the nanoparticles are scattered around SWNTs, and the others are attached onto SWNTs, or wrapped by amorphous carbons (which are by-products during the arc discharge process). Among various purification methods published in literature, chemical oxidation including gas-phase oxidation and liquid oxidation, filtration, centrifugation, high temperature annealing, and ultrasonication are commonly used [8–14]. In recent years, researchers have also tried to use combinations of the above methods for purification [15–21]. However, these methods are intended to be very efficient in removing all impurities. Our developed method selectively keeps nickel nanoparticles, which are firmly attached onto the SWNTs after purification, while scattering nickel nanoparticles and amorphous carbons surrounding the M-CNTs are removed. Nickel nanoparticles remaining on SWNT surface; however, will enable the SWNT to respond to an external magnetic field.

Another innovation in this paper is to use AFM force–distance curve analysis (AFM-FCA) combined with TEM image to monitor the SWNT purification process. An AFM force–distance curve is a plot representing force–distance relationship between AFM tip and the sample surface, and the separation distance is controlled by a closed-loop scanning system of the AFM during the measurements [22]. The interacting force measured in air is usually the van der Waals (VDW) force. AFM-FCA has been applied to obtain information about the electric properties, the elastic modulus, and the chemical bonding strengths of the samples [22]. The curve can be drawn after a complete AFM tip engaging process is performed, which includes an approaching and detaching cycle. When the tip is approaching the sample surface, at one point, the attraction between the AFM tip and sample surface will cause sudden movement of the tip towards the sample surface (so-called jump-in process), leading to a peak value on the curve. Similarly, during the detaching process, the AFM tip remains in contact with the sample surface due to the VDW attractive force until one critical point is reached when the interface separates (so-called jump-out process). This jump-out will lead to another peak value on the force–distance profile. Compared with the peak force in the approaching process, the jump-out peak value in the detaching process is less affected by the tip engaging speed, which corresponds to the force necessary to remove the cantilever tip from the sample surface and is essentially a measure of the adhesive force, thus in this paper only the AFM force curve during the detaching process is presented, and the related peak value is defined as the adhesion force. The main idea is, in this paper, the ranges of adhesion force for three fundamental materials is identified first: (1) the range of adhesion force between the AFM tip and amorphous carbon, (2) the range of adhesion force between the AFM tip and pre-purified SWNT, and (3) the range of adhesion force between the AFM tip and nickel nanoparticles. Then based on the values of the adhesion forces, sample points taken during the different purification treatments will be used to qualitatively differentiate the materials in the mixtures. Compared with TEM, scanning electron microscope (SEM), or Raman spectra which are commonly used to monitor the purification process, this method is fast and intuitive. As previously mentioned, the major impurities in arc-discharged SWNTs are nickel nanoparticles and amorphous carbons [8]. To prove that adhesion force information extracted from AFM-FCA can be used to differentiate the three standard materials mentioned above, an experimental model and numerical hypothesis are provided. The calculation results are in line with our experimental results. To our best knowledge, this is the first report on using AFM-FCA to assist SWNT purification.

## 2. Materials and experiments

### 2.1. Materials

Sodium dodecyl sulfate (SDS) (05030) was purchased from Fluka Analytical<sup>®</sup>. Hydrogen peroxide (H3410) was purchased from Sigma<sup>®</sup>. Polytetrafluoroethylene (PTFE) membrane filter (0.45  $\mu\text{m}$ ) (TE36) was purchased from Whatman<sup>®</sup>. *N,N*-dimethylformamide (DMF) (31,993-7) and amorphous carbon (484164) were purchased from Aldrich<sup>®</sup>. 95% ethanol was purchased from Commercial Alcohols<sup>®</sup>. DI-water was supplied from the university purification system.

Pre-purified SWNTs (652490) used as the standard material were purchased from Sigma<sup>®</sup> and manufactured by the arc-discharge method. The manufacturer claimed that the nanotubes were purified with nitric acid and left in a highly functionalized form.

Arc-discharged raw SWNTs (519308) used in our developed purification process were also purchased from Sigma<sup>®</sup>. Based on the product information, the sample composition is 50–70% carbon, as determined by Raman spectroscopy and SEM. It contained residual catalyst impurities Ni. The SWNTs were in bundles of length  $\sim 20\text{ }\mu\text{m}$ , and individual tube length was unknown.

### 2.2. Instrumentations

Thermo Fisher Scientific<sup>®</sup> Sorvall T1 centrifuge and Fisher Scientific<sup>®</sup> bath sonicator (FS30H) were used in the purification process. Transmission electron microscopy (TEM) images were acquired on a JEOL<sup>®</sup> TEM microscope. Sample solution was sonicated for 10 min and immediately transferred dropwise onto the TEM mesh grid. The TEM sample grid was dried overnight at room temperature. TEM images were photographed on the next day. AFM image and related FCA were performed on a Veeco<sup>®</sup> Multimode V SPM under contact mode. The AFM tip used was Veeco<sup>®</sup> NP-20. Firstly, the pH value of the sample solution was adjusted to approximately 7.0. A small amount of sample solution was then directly transferred dropwise onto the silicon wafer. The sample was dried at room temperature overnight.

#### 2.2.1. Standard materials preparation

Certain amount of amorphous carbon was firstly sonicated in DI-water for 10 min, then directly transferred dropwise on a small piece of silicon wafer. The sample was dried at room temperature.

To further ensure the pre-purified SWNT was pure, SWNT samples were oxidized in concentrated acid (sulphuric acid:nitric acid = 3:1) for 40 min and sonicated in  $\text{H}_2\text{O}_2$  for another 2 h. After being transferred dropwise onto the silicon wafer, the solution was dried at room temperature.

The pure nickel nanoparticles were obtained from a redox reaction between nickel oxalate and formic acid. The remaining sample preparation steps were the same as that for amorphous carbon.

#### 2.2.2. Purification process

The purification process consisted of three treatments: (a) SDS treatment, (b) organic solvent treatment and (c)  $\text{H}_2\text{O}_2$  treatment, which are described in detail as follows:

**2.2.2.1. SDS treatment.** 26.2 mg SWNTs were weighed and dispersed in a solution of 10 mL 20% concentration SDS and 150 mL DI-water. The container was gently agitated, and then the sample solution was sonicated for 2 h. After sonication, sample solution was transferred into centrifuge tubes and centrifuged at 10,000 rpm for 10 min. Sediment was discarded; supernatant was filtered through a PTFE membrane with 0.45  $\mu\text{m}$  pore size. In order to completely remove the SDS after filtration, DI-water was used to wash the SWNTs remaining on the filter membrane over several rinse cycles. Finally, SWNTs remaining on the PTFE membrane were suspended in 95% ethanol. Sample solution was stored at room temperature for TEM analysis and the next purification treatment.

**2.2.2.2. Organic solvent treatment.** Before organic solvent treatment, the sample solution needs to be completely dried. After the drying process, SWNTs were suspended in 100 mL DMF, after which the sample solution was refluxed at 130  $^\circ\text{C}$  for 98 h. After the reflux process, the sample solution was filtered again through a PTFE membrane with 0.45  $\mu\text{m}$  pore size. DI-water was used to wash away the remaining DMF. SWNT remaining on the PTFE membrane was suspended in 95% ethanol and stored properly for TEM and AFM analysis and the next purification step.

**2.2.2.3.  $H_2O_2$  treatment.** Before  $H_2O_2$  treatment, sample solution needs to be completely dried. After the drying process, 22 mL  $H_2O_2$  was added to suspend SWNTs. The sample solution was then sonicated for a total duration of 4 h. To ensure enough oxidant was supplied 10 mL  $H_2O_2$  was supplemented into the solution at 2 h intervals. After  $H_2O_2$  treatment, samples underwent the same filtration process as previously described. Finally, SWNT could be stored in 95% ethanol solution.

### 3. Results and discussion

In order to use the defined adhesion force to differentiate materials, it should be proven that the ranges of adhesion forces associated with different materials have little overlap with one another in this case. Both experimental and theoretical approaches have been carried out in order to reach a convincing conclusion.

#### 3.1. Experimental evaluation of adhesion force

The adhesion force between the AFM tip and pure standard materials by AFM-FCA was determined in contact mode. The AFM tip was approaching and detaching from the sample surface at a rate of 1 Hz. During the experiments, an AFM topographic image reflecting the sample's surface structure was first generated. As the adhesion force depends on the geometry and size of interacting surfaces, the rules to choose the sample points from the generated AFM image are universal throughout the standard material analysis. The rules are, (a) the morphology feature is clear on the image, (b) the surrounding morphology of the sample points is similar, such as slope and particle size. In reality, it was hard to keep sampling consistent even in the same material. Therefore, instead of using only one force value, a range of adhesion force values was identified for each material. The real "separation distance" between the AFM tip and sample surface is the combined effect of several factors, such as the chemical composition of the material, the chemical composition of the tip, the morphology of the material surface, the morphology of the tip, and the detaching speed. Because many of these involving factors can vary, this is a sensitive process. Therefore, it is hard to accurately measure the range of the separation distance. To summarize adhesion force from the sample points, Fig. 3a–c are presenting in the following way, the vertical axis represents for the value of adhesion force, while the horizontal axis represents the AFM tip ramp size when the peak adhesion force is obtained which is termed ramp size at jump-out. As shown in Fig. 1a, in the approaching process, the AFM tip started in air at 0 nm and then moved 1  $\mu$ m to reach the material surface, but this process doesn't guarantee the tip will just touch the material surface after 1  $\mu$ m. During the detaching process, as shown in Fig. 1b, the "turnaround" point, where the tip is going to be lifted, is defined as 0 nm, and from then on the ramp size is measured in the opposite direction. Because only the detaching process is presented in this manuscript, the ramp size in all related images is

measured from the "bottom". For Figs. 5, 7 and 8, the vertical axis is the same as mentioned above, but the horizontal axis shows the overall ramp process during the detaching process.

##### 3.1.1. Adhesion force on amorphous carbon

The AFM image information of amorphous carbon is presented in Fig. 2a–c. Fig. 2a shows the overall amorphous carbon structure, while Fig. 2b presents this surface morphology in a 3D view. Fig. 2c demonstrates the sample points that have been used for AFM-FCA. They are marked by red dots. Fig. 3a summarizes the adhesion forces from all the sample points. As mentioned above, to keep a relative consistent sampling environment, all the sample points were taken on one carbon bump, which was measured to be spherical with a radius of 1  $\mu$ m from Fig. 2c. From Fig. 3a, majority of the values of the adhesion force for amorphous carbon range from 26.9 to 38.7 nN with an average of 31.7 nN. It should be mentioned that there is one point measured to be about 22.8 nN far away from the majority. The micro-scale morphology variance may lead to a relative wide range of AFM tip ramp size. For the other two standard materials, the experiment results presented from Fig. 2d–i are listed in the same way.

##### 3.1.2. Adhesion force on SWNT

The SWNTs' radius was measured to be 87, 92.2, 108, 123, or 130 nm from Fig. 2f, thus the SWNTs exist in bundled form in this case. SWNTs are supposed to have a relative uniform morphology, which is proved by experimental results. The variance in adhesion force is much smaller compared to amorphous carbon as shown in Fig. 3b. The adhesion force values range from 21.8 to 26.8 nN with an average of 23.9 nN. In addition, the range of the ramp size at jump-out is smaller.

##### 3.1.3. Adhesion force on nickel nanoparticles

As seen in Fig. 2g, there are many nickel nanoparticles, but the radius for nickel nanoparticles could be divided into 27.5, 55, 111 and 222 nm according to Fig. 2i. The range of adhesion force for nickel is from 6.8 to 21.3 nN with an average of 16.4 nN. The pattern of adhesion force scattering of nickel nanoparticles is similar to the one for amorphous carbon as presented in Fig. 3c, but the variance in the value of adhesion force is larger. Because nickel is metallic, not only the morphology difference will lead to the variance in adhesion force, crystal orientation also plays an important role in determining the adhesion force values [23].

In order to compare the range of adhesion force for different materials, the overall adhesion force scattering is shown in Fig. 3d and e. For Fig. 3d, the vertical axis represents the value of adhesion force, while the horizontal axis represents the AFM tip ramp size at jump-out. For Fig. 3e, the vertical axis shows the value of the adhesion force, while the horizontal axis is the sample's serial number. As shown in both Fig. 3d and e, based on the density of the points for each material, there are clear distinctions among these three materials except for the single exceptional point from

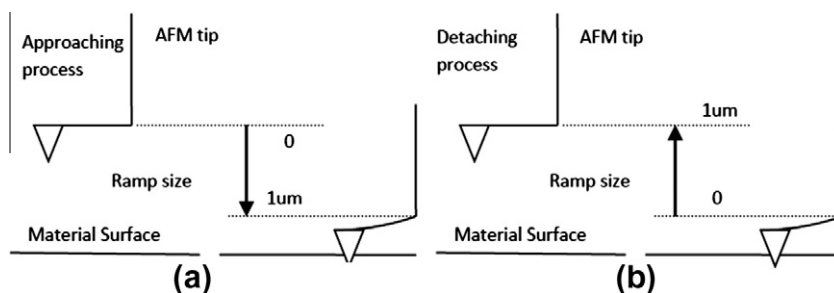
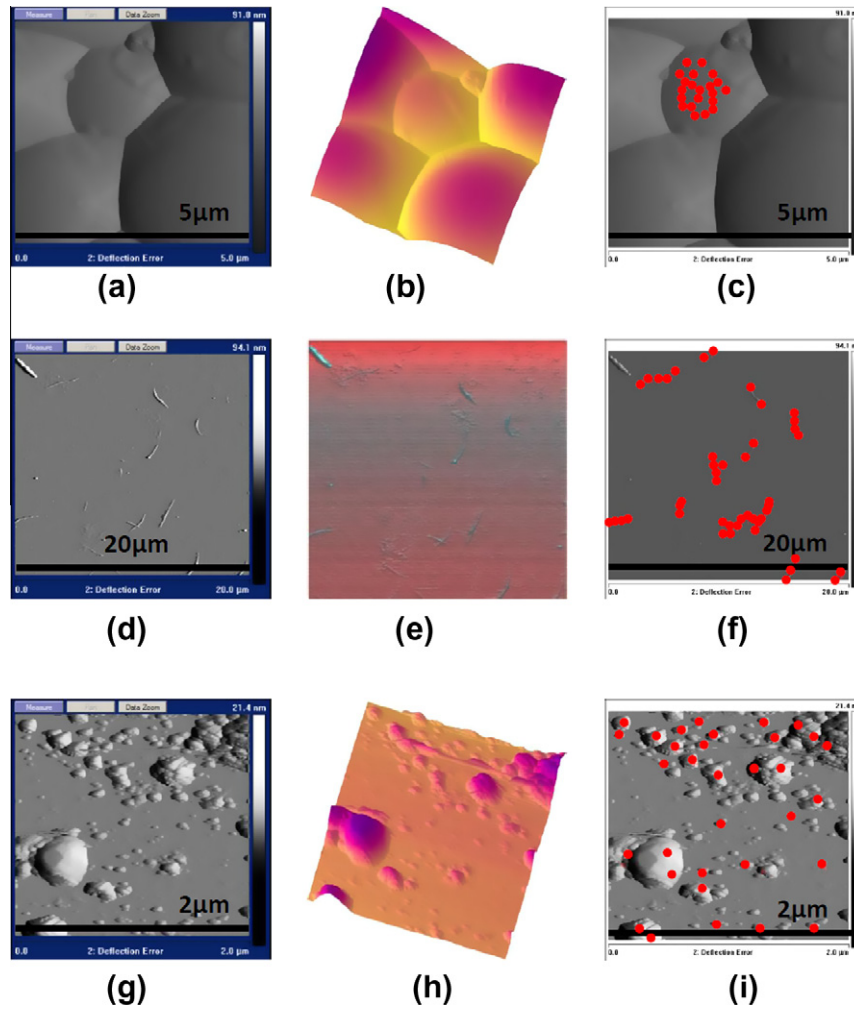


Fig. 1. (a) AFM tip approaching process, the ramp size was measured from top to bottom. (b) AFM tip detaching process, the ramp size was measured from bottom to top.



**Fig. 2.** (a) AFM deflection image of amorphous carbon; (b) 3D image of amorphous carbon; (c) point image of amorphous carbon, red dots represent the sampling point; (d) AFM deflection image of SWNT; (e) 3D image of SWNT; (f) point image of SWNT, red dots represent sample points; (g) AFM deflection image of nickel nanoparticles; (h) 3D image of nickel nanoparticles; and (i) point image of nickel nanoparticles, red dots represent sample points.

amorphous carbon. The range of adhesion force is 28–38 nN for amorphous carbon, 22–26 nN for bundled SWNTs, and 6.8–20 nN for nickel nanoparticle. These non-overlapping force ranges provide an effective means to differentiate the three materials from AFM adhesion force measurements. It should be noted that the force measurement in our experiments is very accurate. Specifically, the normal distance resolution of the AFM was 0.1 nm. The spring constant of the cantilever used in the force measurement was 0.27 N/m for amorphous carbon, 0.30 N/m for SWNTs and 0.28 N/m for nickel, therefore the force sensitivity is <0.1 nN.

### 3.2. Theoretical evaluation of adhesion force

It is known that the Johnson–Kendall–Roberts (JKR) theory can be used to predict the force needed to separate a particle from another particle or a flat surface [24]. This model is widely used but requires the deformation of the interacting particles to be small. To simply estimate the defined adhesion force between the AFM tip and the material, the calculation contains the following steps: (a) choose the interaction model determined by the JKR theory, (b) measure the size of the two interacting particles from the AFM deflection image, (c) identify the Hamaker constants based on existing literature, and (d) calculate the adhesion force using the following equations from the JKR theory:

$$F_{ad} = 3\pi R \frac{W_{ad}}{2} \quad (1)$$

$$R = \frac{R_1 R_2}{R_1 + R_2} \quad (2)$$

$$W_{ad} \approx \frac{A_{12}}{12\pi D_0^2} \quad (3)$$

$$A_{12} = \sqrt{A_1 A_2} \quad (4)$$

where  $F_{ad}$  is the defined adhesion force between two spherical particles,  $R_1$  and  $R_2$  are the radii of curvature of the interacting particles;  $W_{ad}$  is the work of adhesion;  $A_1$ ,  $A_2$ , and  $A_{12}$  are the Hamaker constants and  $D_0$  is the closest separation between the two particles. In the following calculation,  $R_1$  stand for the radius of the sample material which was determined by the pixel method. For example, the scale bar takes 100 pixels, and thus a SWNT's diameter, which takes 50 pixels, will be half of the scale bar.  $R_2$  stand for the radius of the AFM tip.  $D_0$  is chosen to be 0.16 nm from Jacob Israelachvili's book "Intermolecular and Surface Forces" [25]. Based on this separation, Eq. (3) has been successfully applied to predict the surface and adhesion energies of a variety of compounds ranging from simple molecular materials to polymers. This separation should also be close to the real contact separation between the



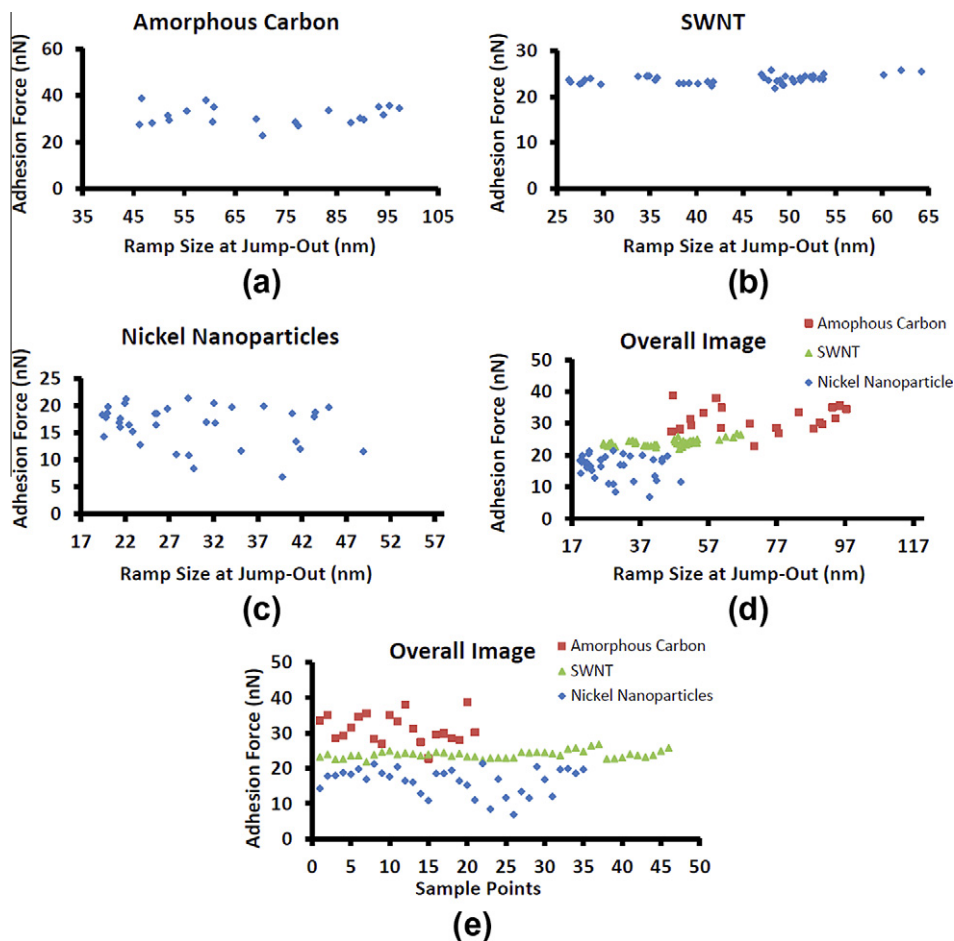


**Fig. 3.** (a) Adhesion force vs. ramp size for amorphous carbon; (b) adhesion force vs. ramp size for SWNT; (c) adhesion force vs. ramp size for nickel nanoparticles; (d) overall image of adhesion forces of amorphous carbon, CNT and nickel nanoparticles vs. ramp size; and (e) overall image of adhesion forces of amorphous carbon, CNT and nickel nanoparticles vs. sample points.

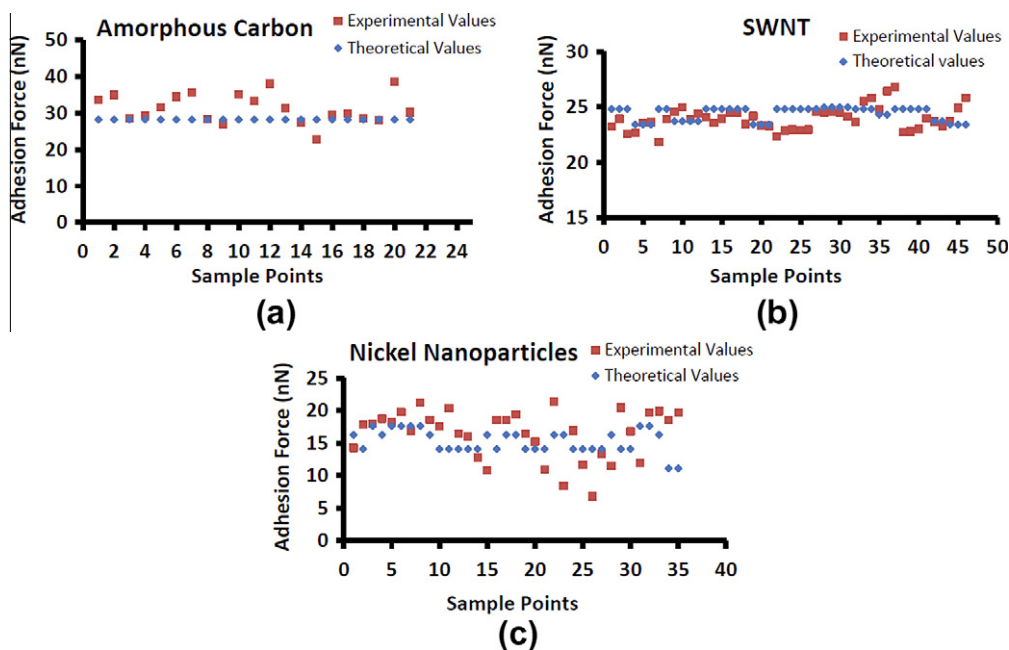


**Fig. 4.** (a) Adhesion forces of amorphous carbon, experimental values vs. theoretical values; (b) adhesion forces of SWNTs, experimental values vs. theoretical values; and (c) adhesion forces of nickel nanoparticles, experimental values vs. theoretical values.

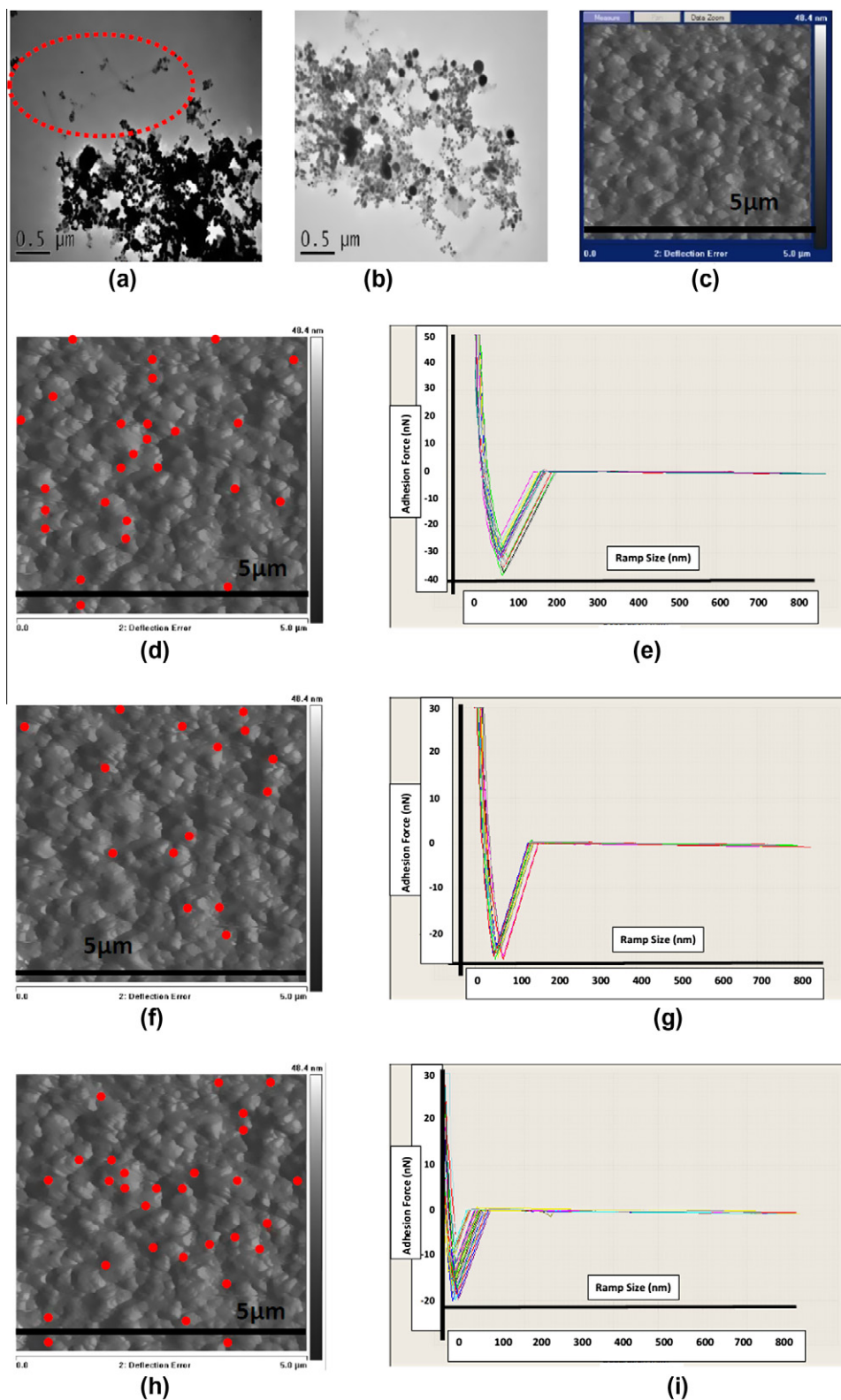


**Fig. 5.** (a and b) TEM image of the original SWNTs; (c) AFM deflection image of the original SWNTs; (d and e) AFM-FCA of original SWNT, sample points represent amorphous carbon; (f and g) AFM-FCA of original SWNT, sample points represent SWNT; and (h and i) AFM-FCA of original SWNT, sample points represent nickel nanoparticle.

molecules/atoms on the AFM tip and the contacting molecules on the opposing sample surface.

### 3.2.1. AFM tip interacting with amorphous carbon surface

According to Fig. 2b, the amorphous carbon has a spherical structure, since the AFM tip is simplified as a sphere, thus the sep-

aration process is approximated as two spherical surfaces locally interacting with each other. All the sample points were taken on one carbon bump, and it was measured to be spherical with radius ( $R_1$ ) of 1 μm, while the tip radius ( $R_2$ ) is around 20 nm. From the literature [26], the Hamaker constant for amorphous carbon and  $\text{Si}_3\text{N}_4$  are  $A_1 = 50 \times 10^{-20}$  and  $A_2 = 17.4 \times 10^{-20}$  J, respectively.

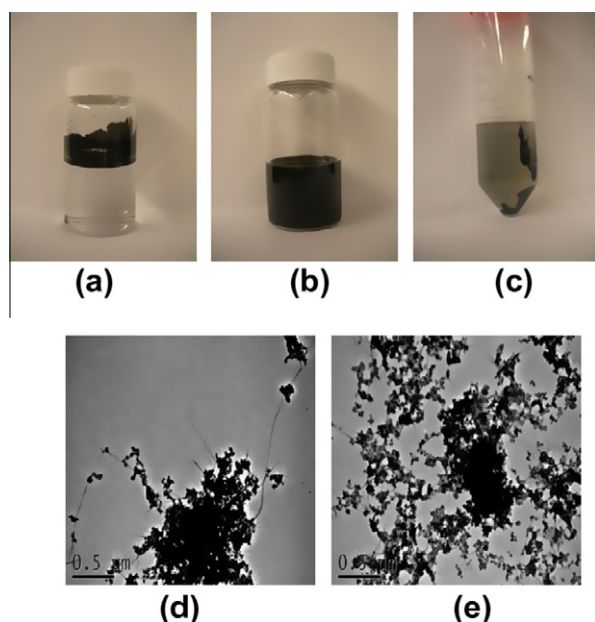


**Fig. 6.** Experiment process of SDS treatment (a) original SWNT in DI-water; (b) original SWNT mix with SDS; (c) SWNT solution after centrifugation; and (d and e) TEM image of SWNT after SDS treatment.

The calculated adhesion force for amorphous carbon is 28.2 nN. Fig. 4a compares experimental values with theoretical values for amorphous carbon. The vertical axis stands for the value of adhesion force, while the horizontal axis is the sample point serial number. Clearly the theoretical value falls into the range of adhesion force measured experimentally.

### 3.2.2. AFM tip interacting with SWNT surface

The SWNTs' radius ( $R_1$ ) was measured to be 87, 92.2, 108, 123, or 130 nm, thus the SWNTs in our sample are obviously in bundled form. Although the bundled SWNTs are best approximated by a cylindrical structure, the exact JKR solution for the adhesion force between a sphere and a cylinder is not available. Therefore, here we approximate the bundled SWNTs by a sphere and use Eq. (1) to estimate the adhesion force. More accurate calculation of adhesion force between a sphere and a cylinder can be obtained through numerical analysis, for example, using finite element method. However, this is out of the scope of this work. According to this, the bundled SWNTs are considered as a sphere; while the AFM tip represent the other sphere. The tip radius ( $R_2$ ) is around 20 nm. The Hamaker constants for CNT and  $\text{Si}_3\text{N}_4$  are  $A_1 = 50 \times 10^{-20}$  and  $A_2 = 17.4 \times 10^{-20}$  J [26]. The calculated adhesion force for bundled SWNTs is 23.4, 23.7, 24.3, 24.8, and 24.9 nN. Fig. 4b compares experimental values with theoretical values for SWNTs. Most of the theoretical values agree well with experimental values.

### 3.2.3. AFM tip interacting with nickel nanoparticle surface

The nickel nanoparticles are simplified to have a spherical structure. This process is also approximated as two spherical surfaces interact locally. The radius for nickel particle ( $R_1$ ) could be classified into 27.5, 55, 111 and 222 nm, while the tip radius ( $R_2$ ) is 20 nm. The Hamaker constants for nickel and  $\text{Si}_3\text{N}_4$  are  $A_1 = 22 \times 10^{-20}$  and  $A_2 = 17.4 \times 10^{-20}$  J [25]. The calculated adhesion force for nickel nanoparticles with different size is 11.1, 14.1, 16.3 and 17.6 nN respectively, which is in line with the experimentally measured values.

We have shown from both theoretical analysis and experimental measurements that, there is a clear difference in adhesion force for these three materials. Therefore, we consider the exceptional point in amorphous carbon to be abnormal, and it will not be considered in the following analysis. In all, the experimental measurement is in accordance with the theoretical calculation. To explain the difference between theoretical value and experimental value, in addition to the reasons previously mentioned, another two possible factors are: (a) in the theoretical analysis, all the samples are assumed to have a round morphology or at least a round cross area, which is not always true in the experiments (b) in the theoretical calculations, the tip is assumed to interact with the middle of the samples. However, this is difficult to control in experiments. Some of the sample points are not located in the center of the particle.

Although there are obvious differences in the adhesion forces for these three materials, one thing that should be noticed is that in our simple theoretical calculation, it is the size difference that allows us to distinguish the amorphous carbon from SWNT. In the purification process, there is in fact a clear distinction between the size of aggregated amorphous carbon and bundled SWNT. Although sometimes the materials' size can change due to external force, if properly sampled, the morphology around the sample location is quite consistent for each material. Therefore, in general, we can use the adhesion force to distinguish these three different materials on the same substrate. By comparing with the ranges of adhesion force identified for the three standard materials, we can separate the materials in the mixture based on its adhesion force value. We have used this method to monitor the SWNT purification process.

## 3.3. Purification process

TEM and AFM-FCA were performed at different purification steps. The aim is to monitor the process and judge which material is removed or being changed status after the respective process.

### 3.3.1. Original SWNT material

Fig. 5 shows the status of original arc-discharged raw SWNT material before any purification. Fig. 5a and b were taken by TEM, while Fig. 5c was taken by AFM. In Fig. 5a, some SWNTs are visible in separated state as outlined in red dash line. However, single SWNT is difficult to locate in Fig. 5b. We speculate that most of SWNTs are entangled by amorphous carbon (grey block) and wrapped by nickel nanoparticles (dark points). Comparing Fig. 5c with Fig. 5a, it is even more difficult to differentiate SWNTs from the impurities.

AFM-FCA was performed in the scanning area and the data for all these three materials are shown from Fig. 5d–i. According to the specific range of adhesion force values for associated standard material, we can separate the data into three sections with each one standing for one standard material. For instance, all the points marked by red dots in Fig. 5d represent amorphous carbon with adhesion force range from 28.8 to 38.3 nN, while the red dots in Fig. 5f and h represent SWNTs with the adhesion force range from 23.1 to 25.3 nN and nickel nanoparticles with the adhesion force range from 7.5 to 20 nN, respectively. After AFM-FCA, compared with information extracted from TEM images shown in Fig. 5a and b, more direct and detailed information about the material distribution in the accumulation area is obtained. Comparing the distribution of the three materials on the substrate, it is confirmed that the SWNTs are surrounded by the amorphous carbon and nickel nanoparticles.

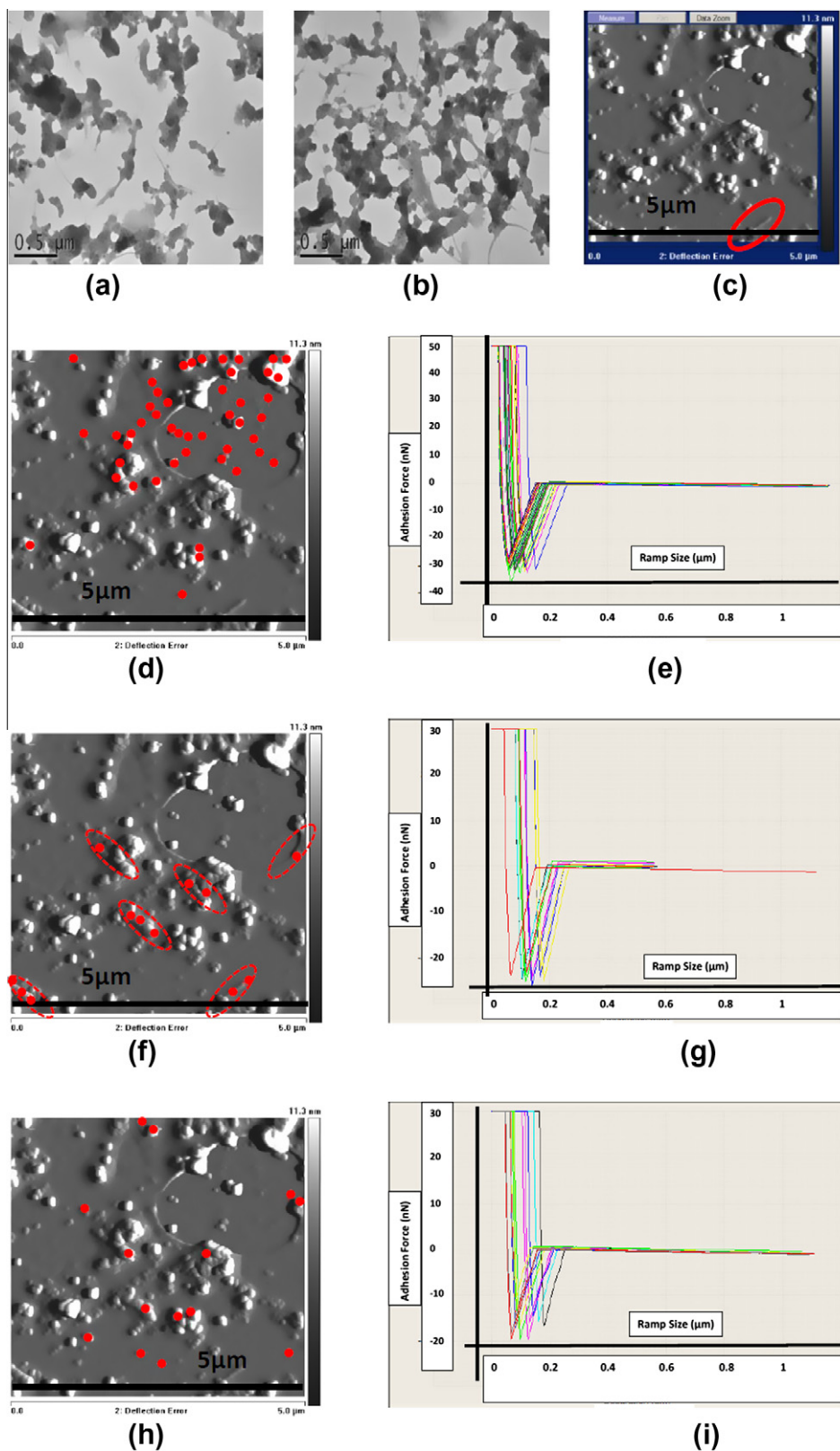


**Fig. 7.** (a and b) TEM image of SWNT after organic solvent treatment; (c) AFM deflection image; (d and e) AFM-FCA of SWNT after organic solvent treatment, sample points represent amorphous carbon; (f and g) AFM-FCA of SWNT after organic solvent treatment, sample points represent SWNT; and (h and i) AFM-FCA of SWNT after organic solvent treatment, sample points represent nickel nanoparticles.

### 3.3.2. Sample after SDS treatment

Fig. 6 presents the status of SWNT during the SDS treatment. Fig. 6a shows that the original SWNTs are not water soluble. SDS

is a highly effective surfactant and is used here to assist the dispersion process. Sonication further disperses the accumulation of amorphous carbon and nickel nanoparticles. It is assumed that



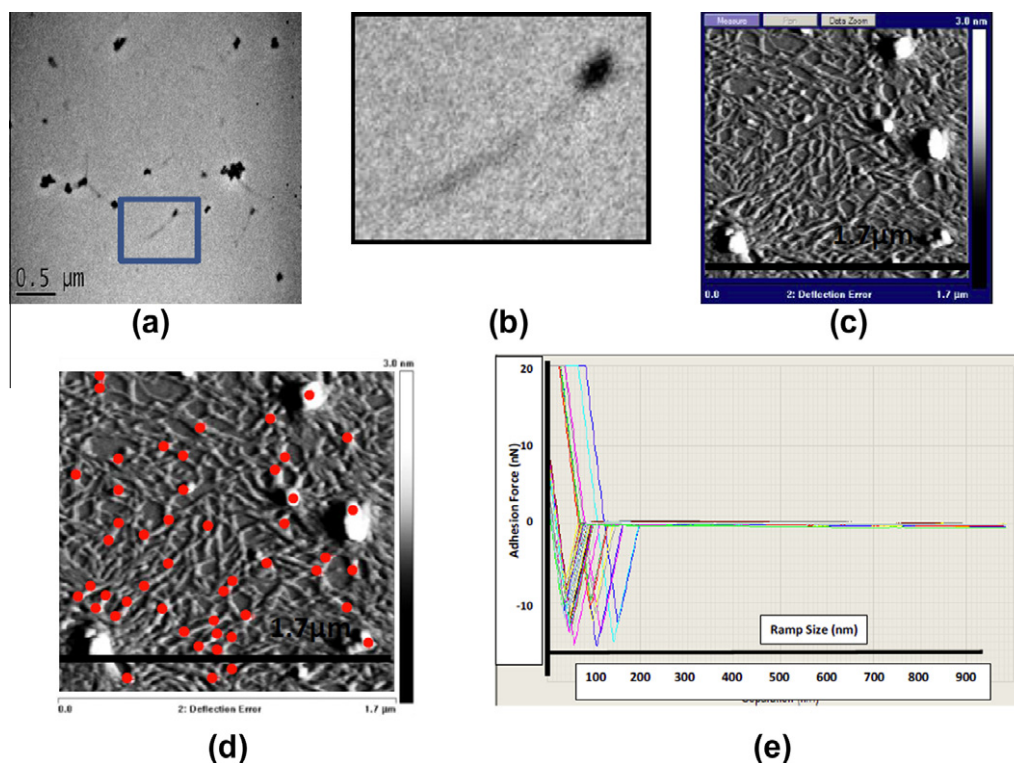


**Fig. 8.** (a and b) TEM image and (c) AFM deflection image of SWNT after  $\text{H}_2\text{O}_2$  treatment; (d and e) AFM-FCA of SWNT after  $\text{H}_2\text{O}_2$  treatment, sample points represent nickel nanoparticles.

SDS will quickly surround the separate nanoparticles to make them water soluble after sonication has fragmented the accumulated block shown. The resulting SWNTs are temporarily dispersed in the solution as presented in Fig. 6b. However, some impurities are too large and heavy for SDS to ensure good solubility. By centrifuging the solution at 10,000 rpm, many large impurity particles are supposed to be removed as shown in Fig. 6c. Fig. 6d and e show the TEM images of SWNTs after the SDS treatment. More SWNTs are observed, again supporting our hypothesis that SWNTs were initially embedded in the accumulation of impurities.

### 3.3.3. Sample after organic solvent treatment

Fig. 7a–c presents the SWNT distribution and morphology after organic solvent treatment. Fig. 7d–i present the AFM-FCA result. After organic solvent treatment, the condition of SWNTs has greatly changed. With TEM technology, Fig. 7a and b show that the accumulation blocks have been further divided into smaller pieces, while many SWNTs still entangle. The amorphous carbons now exhibit loose structures. Fig. 7c which is taken by AFM shows lots of small particles while one bundled SWNTs marked out by red circle can be directly identified in the right bottom corner.

Although DMF is usually used to disperse SWNTs [27], it is suspected that DMF can cause the impurity accumulation to be fluffy. From the block morphology shown in Fig. 7a and b, more and more organic solvents are adsorbed into the accumulation blocks, leading to further loosening of the accumulation structure. Since amorphous carbon is no longer firmly packed, it will be easier to release the SWNTs entrapped.

AFM image also validates our speculation. Sonication breaks the accumulation into lots of separated nanoparticles. Based on AFM-FCA measurement shown in Fig. 7d, e, h, and i, these nanoparticles are composed of nickel nanoparticles or amorphous carbons. For the amorphous carbon sample points, the adhesion force is from 28.2 to 36 nN, while for nickel nanoparticles, the adhesion force

range from 11.3 to 19.8 nN. As mentioned above, in the right bottom of Fig. 7c, we can clearly identify one tube by its morphology. For other tubes, we cannot differentiate the whole structure purely from the morphology, but AFM-FCA provides additional information about the embedded SWNTs. Fig. 7f shows the sample points representing SWNT. The adhesion forces on these SWNTs range from 22.5 to 26 nN. The overall morphology of SWNTs are estimated and marked in red dashed circle. These SWNTs are not totally purified. According to Fig. 7c, some small accumulations still exist on the SWNTs' surface. Based on AFM-FCA result shown in Fig. 7d and h, dots sampled on these accumulations are associated with amorphous carbon and nickel nanoparticles which indicate that the SWNTs are covered by the impurity.

### 3.3.4. Samples after $\text{H}_2\text{O}_2$ treatment

Feng has shown that  $\text{H}_2\text{O}_2$  could help oxidize amorphous carbon at room temperature [28]. Since after organic treatment, amorphous carbons have become loose scaffolding, it turns out to be much easier to remove them. Fig. 8a–c presents the distribution and morphology of SWNT, while Fig. 8d and e show the result of AFM-FCA. After the  $\text{H}_2\text{O}_2$  treatment, which is the last purification stage, most amorphous carbons and scattering nickel nanoparticles are removed, and thus SWNTs are free in solution with nickel nanoparticles attached onto their surface. As Fig. 8a shows, there is almost no amorphous carbon left in the solution. Short SWNTs are observed for the first time and they are evenly distributed in the image. Most SWNTs have a dark point in the tip indicating the presence of nickel nanoparticles. The magnification of specific SWNT is shown in Fig. 8b.

From the AFM image shown as Fig. 8c, we can identify lots of SWNTs, but in addition to SWNTs, there are some large particles existing in the solution. From Fig. 8d and e, AFM-FCA classifies these large particles to be nickel nanoparticles because the values of defined adhesion forces on the large particles range from 8.9 to

15.5 nN which drop into the experimentally measured adhesion force range for nickel nanoparticle. Since the SWNT sample solution has gone through three filtration stages, most of the small nickel nanoparticles existing in the filtrate have been removed. As SWNTs at some point may block the pores on PTFE membrane, some of the large nickel particles may still remain in the sample solution.

At red dots shown in Fig. 8d, adhesion forces on the SWNTs were also fallen into the range for nickel nanoparticles, we believe this is due to the existence of nickel nanoparticles which are still attached onto most of the carbon nanotubes. The nickel particles are added during the SWNT production stage as catalyst. According to Gavillet et al., the SWNTs growth mode is not really understood even though there are some models proposed to explain. Based on Gavillet's research, when the particle diameter is within the order of a few tens of nm, which is definitely our case, a large number of nickel nanoparticles will precipitate on the surface of SWNTs [29]. But Sonication is harsh, especially for prolonged sonication in our case. Therefore, we suspect that, in addition to the precipitate, some catalyst particles are trapped into the tip of SWNT, thus leading to a firm combination. The possibility of this situation is also explained in Gavillet's work [29]. Since nickel is sensitive to a magnetic field, we believe the residing nickel nanoparticles on the SWNTs will make the SWNTs sensitive to a magnetic field. If the SWNT has to be further purified for special need, we could use specially designed oxidation method to remove the remaining nickel from SWNTs. Potential oxidation methods are described in the following literature [30–32].

#### 4. Conclusion

In this paper, we demonstrate an innovative purification method to extract magnetic carbon nanotubes from purchased raw arc-discharged nanotube materials. The process is divided into three main procedures: SDS treatment, organic solvent treatment, and  $H_2O_2$  treatment. To ensure the SWNTs to retain magnetic properties, harsh acid treatment was avoided though it is commonly used in traditional oxidation methods. In addition, AFM-FCA combined with TEM image was applied to monitor the purification process. Our experimental results are in line with the theoretical results. The advantage of this method is that it can directly differentiate materials once the standard material analysis is performed. In summary, we propose a new purification method and a new analysis method which is efficient and reliable for this magnetic carbon nanotube purification process.

#### Acknowledgment

The authors would like to acknowledge the funding supports of NSERC and CIHR joint CHRP Grant, and NSERC engagement Grant.

#### References

- [1] S. Iijima, Helical microtubules of graphitic carbon, *NATURE* 354 (1991) 56–58.
- [2] M. Singh, P.K. Kathuroju, N. Jampana, Polypyrrole based amperometric glucose biosensors, *Sens. Actuator B-Chem.* 143 (2009) 430–443.
- [3] J. Liu, G. Cao, Z. Yang, D. Wang, D. Dubois, X. Zhou, G.L. Graff, L.R. Pederson, J. Zhang, Oriented nanostructures for energy conversion and storage, *ChemSusChem* 1 (2008) 676–697.
- [4] D. Pantarotto, R. Singh, D. McCarthy, M. Erhardt, J.P. Briand, M. Prato, K. Kostarelos, A. Bianco, Functionalized carbon nanotubes for plasmid DNA gene delivery, *Angew. Chem. -Int. Edit.* 43 (2004) 5242–5246.
- [5] H. Gul, W. Lu, P. Xu, J. Xing, J. Chen, Magnetic carbon nanotube labelling for haematopoietic stem/progenitor cell tracking, *Nanotechnology* 21 (2010) 155101.
- [6] G. Korneva, H.H. Ye, Y. Gogotsi, D. Halverson, G. Friedman, J.C. Bradley, K.G. Kornev, Carbon nanotubes loaded with magnetic particles, *Nano Lett.* 5 (2005) 879–884.
- [7] D. Cai, D. Blair, F.J. Dufort, M.R. Gumina, Z. Huang, G. Hong, D. Wagner, D. Canahan, K. Kempa, Z.F. Ren, T.C. Chiles, Interaction between carbon nanotubes and mammalian cells: characterization by flow cytometry and application, *Nanotechnology* 19 (2008) 345102.
- [8] P. Hou, C. Liu, H. Cheng, Purification of carbon nanotubes, *Carbon* 46 (2008) 2003–2025.
- [9] I.W. Chiang, B.E. Brinson, A.Y. Huang, P.A. Willis, M.J. Bronikowski, J.L. Margrave, R.E. Smalley, R.H. Hauge, Purification and Characterization of Single-Wall Carbon Nanotubes (SWNTs) obtained from the Gas-Phase Decomposition of CO (HiPco Process), *J. Phys. Chem. B* (105) (2001) 8297–8301.
- [10] A.G. Rinzler, J. Liu, H. Dai, P. Nikolaev, C.B. Huffman, F.J. Rodriguez-Macias, P.J. Boul, A.H. Lu, D. Heymann, D.T. Colbert, R.S. Lee, J.E. Fischer, A.M. Rao, P.C. Eklund, R.E. Smalley, Large-scale purification of single-wall carbon nanotubes: process, product, and characterization, *Appl. Phys. A-Mater. Sci. Process* 67 (1998) 29–37.
- [11] J.M. Bonard, T. Stora, J.P. Salvetat, F. Maier, T. Stockli, C. Duschli, L. Forro, W.A. deHeer, A. Chatelain, Purification and size-selection of carbon nanotubes, *Adv. Mater.* (9) (1997) 827.
- [12] A. Yu, E. Bekyarova, M.E. Itkis, D. Fakhrutdinov, R. Webster, R.C. Haddon, Application of centrifugation to the large-scale purification of electric arc-produced single-walled carbon nanotubes, *J. Am. Chem. Soc.* 128 (2006) 9902–9908.
- [13] J.M. Lambert, P.M. Ajayan, P. Bernier, J.M. Planeix, V. Brotons, B. Coq, J. Castaing, Improving conditions towards isolating single-shell carbon nanotubes, *Chem. Phys. Lett.* 226 (1994) 364–371.
- [14] H.C. Shim, H.W. Lee, S. Yeom, Y.K. Kwak, S.S. Lee, S.H. Kim, Purification of carbon nanotubes through an electric field near the arranged microelectrodes, *Nanotechnology* 18 (2007) 115602.
- [15] P.X. Hou, S. Bai, Q.H. Yang, C. Liu, H.M. Cheng, Multi-step purification of carbon nanotubes, *Carbon* 40 (2002) 81–85.
- [16] K. Tohji, H. Takahashi, Y. Shinoda, N. Shimizu, B. Jeyadevan, I. Matsuoka, Y. Saito, A. Kasuya, S. Ito, Y. Nishina, Purification procedure for single-walled nanotubes, *J. Phys. Chem. B* 101 (1997) 1974–1978.
- [17] P.X. Hou, C. Liu, Y. Tong, S.T. Xu, M. Liu, H.M. Cheng, Purification of single-walled carbon nanotubes synthesized by the hydrogen arc-discharge method, *J. Mater. Res.* 16 (2001) 2526–2529.
- [18] Y. Fan, A. Kaufmann, A. Mukasyan, A. Varma, Single- and multi-wall carbon nanotubes produced using the floating catalyst method: synthesis, purification and hydrogen up-take, *Carbon* 44 (2006) 2160–2170.
- [19] S. Bandow, S. Asaka, X. Zhao, Y. Ando, Purification and magnetic properties of carbon nanotubes, *Appl. Phys. A-Mater. Sci. Process* 67 (1998) 23–27.
- [20] F. Li, H.M. Cheng, Y.T. Xing, P.H. Tan, G. Su, Purification of single-walled carbon nanotubes synthesized by the catalytic decomposition of hydrocarbons, *Carbon* 38 (2000) 2041–2045.
- [21] H. Zhang, C.H. Sun, F. Li, H.X. Li, H.M. Cheng, Purification of multiwalled carbon nanotubes by annealing and extraction based on the difference in van der Waals potential, *J. Phys. Chem. B* 110 (2006) 9477–9481.
- [22] Veeco Veeco diMultiMode V SPM Instruction Manual, Veeco Instruments Inc.: 2006, Chapter 10.
- [23] M. Radmacher, J.P. Cleveland, M. Fritz, H.G. Hansma, P.K. Hansma, Mapping interaction forces with the atomic-force microscope, *Biophys. J.* 66 (1994) 2159–2165.
- [24] K.L. Johnson, K. Kendall, A.D. Roberts, Surface energy and contact of elastic solids. *Proceedings of the Royal Society of London Series A-Mathematical and Physical Sciences* (324) (1971) 301.
- [25] Israelachvili, In: *Intermolecular and surface forces*, 2nd ed., Academic press, 1992.
- [26] S. Akita, H. Nishijima, Y. Nakayama, Influence of stiffness of carbon-nanotube probes in atomic force microscopy, *J. Phys. D-Appl. Phys.* 33 (2000) 2673–2677.
- [27] Q. Cheng, S. Debnath, E. Gegan, H.J. Byrne, Ultrasound-assisted swnts dispersion: effects of sonication parameters and solvent properties, *J. Phys. Chem. C* 114 (2010) 8821–8827.
- [28] Y. Feng, H. Zhang, Y. Hou, T.P. McNicholas, D. Yuan, S. Yang, L. Ding, W. Feng, J. Liu, Room temperature purification of few-walled carbon nanotubes with high yield, *ACS Nano* 2 (2008) 1634–1638.
- [29] J. Gavillet, A. Loiseau, J. Thibault, A. Maigne, O. Stephan, P. Bernier, TEM study of the influence of the catalyst composition on the formation and growth of SWNT, *AIP Conf. Proc.* 633 (2002) 202–206.
- [30] R. Sen, S.M. Rickard, M.E. Itkis, R.C. Haddon, Controlled purification of single-walled carbon nanotube films by use of selective oxidation and near-IR spectroscopy, *Chem Mater.* (15) (2003) 22 4273–4279.
- [31] E. Dujardin, T.W. Ebbesen, A. Krishnan, M.M.J. Treacy, Purification of single-shell nanotubes, *Adv. Mater.* (10) (1998) 8 611–613.
- [32] Y.H. Wang, H.W. Shan, R.H. Hauge, M. Pasquali, R.E. Smalley, A highly selective, one-pot purification method for single-walled carbon nanotubes, *J. Phys. Chem. B.* (111) (2007) 6 1249–1252.